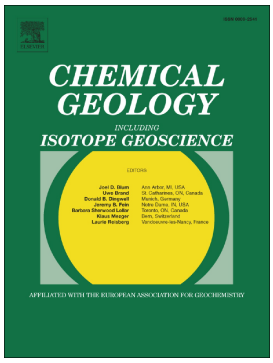

Changes in mineral reactivity driven by pore fluid mobility in partially wetted porous media

A.L. Harrison, G.M. Dipple, W. Song, I.M. Power, K.U. Mayer, A. Beinlich, D. Sinton

PII: S0009-2541(17)30271-1
DOI: doi: 10.1016/j.chemgeo.2017.05.003
Reference: CHEMGE 18332

To appear in: *Chemical Geology*

Received date: 7 January 2017
Revised date: 26 April 2017
Accepted date: 1 May 2017

Please cite this article as: A.L. Harrison, G.M. Dipple, W. Song, I.M. Power, K.U. Mayer, A. Beinlich, D. Sinton , Changes in mineral reactivity driven by pore fluid mobility in partially wetted porous media, *Chemical Geology* (2017), doi: 10.1016/j.chemgeo.2017.05.003

Changes in mineral reactivity driven by pore fluid mobility in partially wetted porous media

A.L. Harrison[a,1*], G.M. Dipple[a], W. Song[b], I.M. Power[a], K.U. Mayer[a], A. Beinlich[a,c], D. Sinton[b]

[a]Department of Earth, Ocean and Atmospheric Sciences, The University of British Columbia, 2207 Main Mall, Vancouver, British Columbia V6T 1Z4, Canada. [*]ALH – anna.harrison@ucl.ac.uk; GMD – gdipple@eoas.ubc.ca; IMP – ipower@eoas.ubc.ca; KUM – umayer@eoas.ubc.ca; AB – andreas.beinlich@curtin.edu.au

[b]Department of Mechanical and Industrial Engineering and Institute for Sustainable Energy, University of Toronto, 5 King's College Road, Toronto, Ontario M5S 3G8, Canada. WS – wensong@stanford.edu; DS – sinton@mie.utoronto.ca

[c]The Institute for Geoscience Research (TIGeR), Curtin University, 6845 Perth, Australia

[1]Present address: Department of Earth Sciences, University College London, Gower Street, London WC1E 6BT, UK

[*]Corresponding author

Highlights

- Gas-water-mineral interface highly dynamic during evaporation in model porous media
- Pore-scale distribution of gas-water mineral interfaces dictates rate and extent of reaction
- Entrainment of reacting mineral particles by the mobile water-gas interface may dramatically alter reactivity
- Particle entrainment process may stimulate mineral precipitation in previously unreactive pores

Abstract

Microfluidics experiments were used to examine mineral dissolution-precipitation reactions under evaporative conditions and identify pore-scale processes that control reaction rate. The entrainment of reacting mineral particles by a mobile water-gas interface driven by evaporation dramatically altered the relative abundance of reactive mineral surface area to fluid reservoir volume. This ratio, which directly influences reaction rate and reaction progress, was observed to vary by nearly two orders of magnitude as evaporation progressed in the experiments. Its dynamic evolution may have a correspondingly large impact on mineral-fluid reaction in Earth's shallow subsurface. We predict that the spatial and temporal variability of pore-scale reaction rates will be significant during evaporation, imbibition, or drainage in the vadose zone, with implications for chemical weathering, soil quality, and carbon cycling. Variable reaction rates during particle mobility are likely to be of increased significance as global rainfall patterns and soil moisture contents evolve in response to climate change.

Keywords: mineral-fluid interface, gas-fluid interface, weathering, wetting-drying cycles, pore-scale processes, evaporation, microfluidics

1. Introduction

Mineral-fluid reactions in Earth's shallow subsurface regulate element transport in nature, disturbed environments, and human-made materials such as industrial wastes. They are vital for nutrient availability, water quality, and carbon cycling (Blowes and Jambor, 1990; Brantley and White, 2009; Maher et al., 2009; Manning, 2008; McKinley et al., 2006). Despite the importance of mineral-fluid reactions in controlling element cycling, predictions of large-scale mass transport are hindered by the scale-dependence of mineral dissolution-precipitation rates and the use of the continuum approach in numerical models that represents porous media with continuous domains of volume-averaged properties (Molins et al., 2012). This approach can lead to significant error in the prediction of geochemical reaction rates (Li et al., 2008, 2006; Molins et al., 2012). As global patterns in rainfall and soil moisture content evolve in response to climate change (IPCC, 2013), the impact of wetting and drying on mineral-fluid reactions is likely to be of increased significance and concern. In particular, unsaturated porous media exhibit highly heterogeneous pore microenvironments that are subject to significant change during gas and fluid mobility. Others have posited that particle entrainment by the mobile fluid meniscus during evaporation or water recharge contributes to hardening of soils, and have shown indirect textural evidence of this process (Bresson and Moran, 1995; Mullins et al., 1987), and Shahidzadeh et al. (2015) demonstrate entrainment of freshly precipitated salt crystals by the retreating air-water interface during unconstrained droplet evaporation. Yet, the chemical impacts of such particle mobility in porous media have not been assessed. We anticipate that pore-scale reaction rates will be highly dynamic and variable in these environments, potentially altering net chemical fluxes

derived from dissolution reactions in porous media, and resulting in heterogeneous distribution of secondary phases.

Experiments using microfluidic reactors (*i.e.*, micromodels) allow visualization of pore-scale processes that can inform development of pore-scale reactive transport models (Boyd et al., 2014; Yoon et al., 2012). To date, most of these experiments have focused on flow dynamics. Only recently have mineral precipitation reactions been studied in water-filled micromodels (Boyd et al., 2014; Yoon et al., 2012; Zhang, 2010) and very few have investigated precipitation in mixed fluid-gas conditions representative of the shallow subsurface (Kim et al., 2013). Here, we consider the reactivity of magnesium hydroxide in the form of the mineral brucite [$Mg(OH)_2$], of interest because of its fast reaction rate at ambient laboratory conditions, because it actively reacts with the atmosphere to sequester carbon, and has recently drawn attention for its potential use for phosphorus recovery from wastewaters (Harrison et al., 2016, 2015, 2013; Hövelmann and Putnis, 2016; Hövelmann et al., 2012; Power et al., 2013; Ulven et al., 2017). We investigated coupled brucite dissolution-carbonate mineral precipitation in a variably water-filled glass micromodel under evaporative conditions to elucidate controls on mineral-fluid reactions and highlight the importance of pore-scale processes on reactivity at conditions representative of the shallow, variably saturated, subsurface.

2. Methods

2.1. Experimental methods

As an example of coupled mineral dissolution-precipitation reactions in the shallow subsurface, duplicate microfluidic brucite carbonation experiments were conducted using an unsaturated silica glass micromodel. Although brucite is not an abundant mineral at the Earth's surface, its rapid reaction rates make it an ideal candidate to observe coupled dissolution-precipitation reactions on an experimental timescale, and it can be utilized to sequester atmospheric CO_2 (Assima et al., 2012; Harrison et al., 2015; Hövelmann et al., 2012; Zhao et al., 2010). The micromodel had a pore network that was 5.0 cm long by 1.5 cm wide with cylindrical glass pillars representative of quartz [SiO_2] grains (Fig. 1). The network consisted of regularly spaced pillars of two sizes: ~180 μm and ~70 μm. Pore throats were between ~215 and 260 μm, the depth was ~130 μm, and the porosity was approximately 0.87. The micromodel was fabricated using standard photolithography techniques and wet etching with hydrofluoric acid (Kim et al., 2013). Prior to experimentation and between experiments, the micromodel was thoroughly flushed with toluene, isopropyl alcohol, 12 M hydrochloric acid, deionized water, and then the experimental slurry. Experimental slurries consisted of 0.5 M $MgCl_2$ prepared using deionized water and reagent grade $MgCl_2 \cdot 6H_2O$, and 5 wt.% pulverized brucite. Slurries were sonicated to minimize particle aggregation prior to injection into the micromodel with a syringe (Song and Kovscek, 2015).

After the slurry was injected, multiple pore volumes of research grade gaseous CO_2 (99.99% purity; Praxair) were flushed through the micromodel to partially displace

the slurry, leaving the pore network with variable water and brucite content (*i.e.*, not all pores were filled with slurry). The micromodel was then immediately connected to a stream of 99.99% purity CO_2 supplied at a constant flow rate of 0.5 mL min^{-1} using a Teledyne ISCO model D-260 pump. A high CO_2 supply rate (0.5 mL min^{-1}) compared to the micromodel pore volume (~85 μL) was utilized to ensure that the carbonation reaction was not limited by a lack of CO_2. The first experiment was conducted for 18 h, and the second for 8 h.

Time lapse greyscale brightfield images were taken at 5 minute intervals during the experiment using an inverted Olympus CKX41 transmitted light microscope (250× objective) and an Orca-ER Hamamatsu camera with resolution of 6.45 μm × 6.45 μm per pixel. ImageJ (Abràmoff et al., 2004) software was used to compile these images into video format (Supporting Information (SI) Videos S1-S2) at 2 frames per second (approximately 10 min of experiment time to 1 s of video). Videos S1 and S2 are a compilation of images collected during the 8 h and 18 h experiment, respectively. The field of view in Videos S1 and S2 are 3.4 mm × 2.2 mm and 1.9 mm × 1.3 mm, respectively. Only the first ~10 h of the latter are included, as little change was observed for the remainder of the experiment. Additional images were collected in color to characterize the entire pore network following the second experiment using a Nikon eclipse E600 POL microscope and Canon EOS Rebel T2i camera. Raman spectra of the reaction products were collected following the second experiment using a Renishaw inVia microscope with 785 nm excitation. Mineral identifications were conducted with reference to the RRUFF^{TM} database of Raman spectra.

In addition to the micromodel experiments, an experiment was conducted to

visualize the behavior of the brucite slurry under the influence of evaporation alone, without the carbonation reaction. In this experiment a brucite slurry of the same composition as that in the micromodels was constrained between two glass slides with its evaporation observed in real time using a Nikon eclipse E600 POL microscope. Photographs were taken periodically with a Canon EOS Rebel T2i camera. The slurry was confined vertically between two glass slides but remained open to the air at the edges of the slides to permit evaporation.

2.2 Characterization and preparation of initial brucite slurry

The brucite was obtained from Premier Magnesia LLC, and was pulverized using a hammermill and subsequently sieved to ≤53 μm in diameter. The particle size distribution was determined using a Malvern Mastersizer 2000 Laser Diffraction Particle Size Analyzer, which indicated that the mean particle diameter was 23 μm. The initial surface area of duplicate samples was determined by multipoint BET with N_2 adsorption using a Quantachrome Autosorb-1 surface area analyzer. It was equal to 5.2 ± 0.2 m^2 g^{-1}.

Rietveld refinement of X-ray diffraction (XRD) data was used to quantify the initial mineralogical composition of the brucite. Triplicate samples were spiked with 10 wt.% highly crystalline CaF_2 to allow quantification of the amorphous (non-crystalline) content (Gualtieri, 2000; Wilson et al., 2006). Samples were ground under ethanol for five minutes using a McCrone micronizing mill and agate grinding elements to reduce the mean particle size. Micronized samples were gently disaggregated with an agate mortar and pestle when dry. The samples were placed in back-loaded cavity mounts against sandpaper to minimize preferred orientation (Raudsepp and Pani, 2003). A Bruker D8

Focus Bragg-Brentano diffractometer with CoKα radiation and a step size of 0.04° over a range of 3-80°2θ at 0.09 s/step was employed. The long fine focus Co X-ray tube was operated using a take-off angle of 6°at 35 kV and 40 mA. DIFFRAC*plus* EVA 14 software (Bruker AXS, 2008) was used for phase identification with reference to the International Centre for Diffraction Database PDF-4+ 2010. Rietveld refinement was performed using Topas Version 3 refinement software (Bruker AXS, 2004). Crystal structure data for brucite (Catti et al., 1995), fluorite (Batchelder and Simmons, 1964), magnesite (Markgraf and Reeder, 1985), lizardite-1T (Mellini and Viti, 1994), hydromagnesite (Akao and Iwai, 1977), dolomite (Ross and Reeder, 1992), and pyroaurite (Olowe, 1995) were used in refinements. Analysis of triplicate samples of the brucite ore indicated it contained 78.8 ± 3.8 wt.% brucite, 5.5 ± 0.4 wt.% dolomite, 1.9 ± 0.3 wt.% magnesite, 7.4 ± 1.0 wt.% hydromagnesite, 5.9 ± 3.3 wt.% amorphous content, and <0.5 wt.% lizardite and pyroaurite.

Brucite slurries were prepared using deionized water and reagent grade $MgCl_2 \cdot 6H_2O$ for a concentration of 0.5 M $MgCl_2$ that was continuously stirred using a magnetic stir plate. Pulverized brucite was added to this solution such that it comprised 5 wt.% of the slurry. A syringe was used to remove an aliquot of the slurry while it was being stirred, and the slurry-filled syringe was briefly sonicated to minimize particle aggregation. The syringe was then used to flush the micromodel with numerous pore volumes of the experimental slurry before the experiment was commenced.

2.3 Geochemical modeling

Geochemical modeling was conducted using PHREEQC V.3 (Parkhurst and Appelo, 2013) to assess the saturation state of carbonate phases, pH changes, and carbonation rate with varying mineral-water interfacial area (MWI). The Pitzer database was used with mineral solubility data from the LLNL database. To predict carbonation rates as a function of changes in mineral-water interfacial area, kinetic brucite dissolution was simulated according to a [HCO_3^-]-dependent kinetic brucite dissolution rate law (Pokrovsky et al., 2005b), assuming equilibrium with pure CO_2 was maintained throughout the reaction. This was justified by the high flushing rate of the gas-filled pore volume in the micromodel with CO_2. Nesquehonite [$MgCO_3 \cdot 3H_2O$] and lansfordite [$MgCO_3 \cdot 5H_2O$] precipitation was simulated at equilibrium, and precipitation of other Mg-carbonate minerals (*e.g.*, magnesite) was suppressed to be consistent with experimental results. The models simulated 10 h of reaction, which is generally consistent with the cessation of reaction due to near complete evaporation of water (estimated between 8 and 12 hours based on time lapse images). To simulate changes in mineral-water interfacial area, the abundance of brucite was altered for a fixed specific mineral surface area equal to the BET-measured surface area, and a fixed volume of water of 1 L.

To examine the potential impact of particle entrainment processes observed in the experiments (section 3.2) on the dissolution of common minerals at the Earth's surface, the kinetic dissolution of calcite [$CaCO_3$], anorthite (Ca-endmember, [$CaAl_2Si_2O_8$]), and quartz [SiO_2] were modeled using PHREEQC V.3. The LLNL database was used, with kinetic dissolution rate laws taken from the literature (Equation 1). Mineral surface areas

were taken from published values for samples used in experiments that determined the mineral's dissolution rate. Specific surface areas of 0.04 m^2 g^{-1} (100-200 µm; Pokrovsky et al., 2005a), 0.09 m^2 g^{-1} (45-125 µm; Gudbrandsson et al., 2014), and 0.11 m^2 g^{-1} (74-149 µm; Brady and Walther, 1990) were used for calcite, anorthite, and quartz, respectively. Calcite, anorthite, and quartz dissolution were simulated according to kinetic dissolution rate laws from Chou et al. (1989), Gudbrandsson et al. (2014), and Brady and Walther (1990) at room temperature. For calcite, quartz, and anorthite, the dependence of the reaction rate on reaction affinity was assumed to follow a transition state theory rate law of the form proposed by Aagaard and Helgeson (1982). Thus, the general form of the equation used for kinetic dissolution of each of these phases was:

$$r = Sk\,\{A\}^n\,(1 - \Omega^b) \qquad \text{Eq. 1}$$

where r is the rate, S is the surface area, k is the kinetic dissolution rate constant, n is the reaction order, and A is an aqueous species upon which the dissolution reaction depends. In the case of anorthite, this is replaced by the term: $\left(\frac{\{H^+\}^3}{\{Al^{3+}\}}\right)$. Finally, Ω is the saturation ratio, defined as the ratio of the ion activity product to the equilibrium constant. The exponent, b is equal to 1 for each mineral except brucite, for which it equals 2 (after Pokrovsky and Schott, 2004). The mineral phases were only dissolved, not precipitated in the models.

3. Results

3.1 Identification of secondary minerals

Real time videos and images collected post-experiment revealed that injection of pure CO_2 gas into the brucite-bearing micromodels induced evaporation of water, disappearance of some brucite particles, and precipitation of secondary minerals of two different morphologies, prismatic and pseudo-rhombohedral (Videos 1-2, Figs. 2 and 3). Raman spectroscopy indicated that a large portion of the precipitates were the hydrated Mg-carbonate, nesquehonite, typified by a prismatic habit consistent with previous studies (Power et al., 2009) (SI Video S1; Figs. 2 and 4). Dypingite $[Mg_5(CO_3)_4(OH)_2 \cdot 5H_2O]$ was also detected (Fig. 4), and was likely a dehydration product of pseudo-rhombohedral crystals interpreted to be lansfordite that disappeared prior to analysis via Raman spectroscopy (Fig. 3; SI Video S2). The pseudo-rhombohedral crystals were consistent with the morphology of lansfordite formed in our laboratory from natural water collected from a Mg-carbonate playa in Atlin, British Columbia, where lansfordite precipitation has previously been documented (Fig. 3; Power et al., 2014). The lansfordite precipitated from water collected at the Atlin site while in storage at 4°C. This dehydration of hydrated carbonate minerals to less hydrated forms has been observed previously to occur in solution (Dong et al., 2008) and during storage under ambient conditions in our laboratory (Power et al., 2016).

The distribution and morphology of precipitates appeared to be dictated by both the local abundance of brucite and the location of the gas-water interface (Fig. 2A, C). Brucite particles in gas-filled pores exhibited no visible signs of carbonation at the scale

of observation (SI Video S1 and Fig. 2E). Interestingly, the morphology of carbonate precipitates in the vicinity of the gas-water interface tended to mimic the curvature of the interface, suggesting their growth may have been limited by the location of this interface (Fig. 2A). In addition, in water-filled zones with high brucite abundance, numerous small crystals of nesquehonite (~200 μm) tended to form, whereas large, single crystals (~1000 μm) were commonly observed in areas with a lower density of brucite particles (Figs. 2C and 2D).

3.2 Estimation of the magnitude of the mineral-water interfacial area

The magnitude of the mineral-water interfacial area was observed to change over time, due both to evaporative water loss and the entrainment of brucite particles by the mobile gas-water interface. To calculate the change in mineral-water interfacial area with time, ImageJ (Abràmoff et al., 2004) software was used to estimate the areal percent of images that were occupied by brucite versus water. Images were segmented by color threshold values chosen manually based on visual identification of water versus brucite grains and the "default" threshold method in ImageJ. The aggregate area of features with values below the threshold were then calculated using the "analyze particles" feature of ImageJ. Figure 5 illustrates the areas that were calculated as water from two representative sections of equal size from an image collected during evaporation of a 5 wt.% brucite slurry between two glass slides (Fig. 6). The stacking of particles in the 3D volume made it impossible to differentiate between particles at different depths within the slurry. Therefore the areal percent was equated to the volume percent occupied by mineral grains. The relative change in volume percent calculated based on these images represents a minimum change, and is an order-of-magnitude calculation due to

uncertainties in grain stacking and thresholding. Based on these images, the volume occupied by brucite for a constant bulk volume increased from 10 to 95 vol.%, equivalent to an ~180-fold increase in the mineral-water interfacial area (MWI) in the evaporation experiment (Figs. 5B and 5C). An ~80-fold increase in MWI is estimated if the bulk areal percent of the slurry prior to evaporation (Fig. 6A), rather than the smaller section in the interior of the evaporated slurry is compared to the same section of the brucite-rich zone (Fig. 5B). The volume percentage occupied by brucite was converted to MWI (m^2 mineral m^{-3} fluid) by normalizing all vol.% values to 1 L of fluid, and calculating the surface area of the brucite in 1 L of fluid at a given vol.% using the density of brucite and the measured BET surface area of brucite.

3.3 Estimation of experimental carbonate growth rate

The carbonate growth rate was estimated based on the rate of growth of the rhombohedral carbonate crystal, presumed to be lansfordite, in SI Video S2. The regular shape and relatively unobstructed view of this carbonate precipitate facilitated calculation of the growth rate, in comparison to the precipitates observed in SI Video S1, which had more complex geometries and were obscured by brucite particles. Crystal growth rates were calculated based on the difference in crystal size between images collected at different points in time, according to the following equation:

$$r = \frac{a(V_2 - V_1)}{(t_2 - t_1)} \div V_w V_m \qquad \text{Eq. 2}$$

where r is the carbonate precipitation rate (mol CO_2 s^{-1} L^{-1}), a is the stoichiometric ratio of the moles of CO_2 consumed per mole carbonate formed, in this case equal to 1 for

lansfordite precipitation, t_1 and t_2 are the experimental time at which a given image was collected (s), V_1 and V_2 are the volume of carbonate at t_1 and t_2 (cm^3), respectively, V_w is the volume of water in the image taken at t_2 (L), and V_m is the molar volume of the carbonate, in this case lansfordite ($cm^3\ mol^{-1}$). The area occupied by the carbonate crystal was calculated with ImageJ by visual identification of crystal edges. The volume of carbonate was estimated assuming the crystal occupied the full depth of the micromodel (~130 μm), with the surface area of the visible crystal face multiplied by the depth of the micromodel. Similarly, the area of the water-filled pore volume within which the crystal resided was calculated using ImageJ via visual identification of the gas-water interface; micromodel pillars were exluded from the water volume. Again, it was assumed that water occupied the full depth of the micromodel. This assumption is justified as water is the wetting fluid under these conditions. The water volume was determined by multiplication of the surface area of the visible water and the depth of the micromodel. Five frames between 90 and 245 min of the experimental duration in SI Video S2 (~9 s and 24 s video time) were selected, with the rate calculated between each frame.

In order to normalize these rates to the mineral-water interfacial area, the mineral-water interfacial area was estimated for the last frame used in the rate calculations (245 min experimental time) because the distribution of brucite was relatively homogeneous throughout the water-filled pore at this time (Video S2). The MWI was estimated using ImageJ as previously described. It was assumed that the total mass of brucite in this pore remained relatively unchanged throughout the experiment, as is consistent with observation. Moreover, based on the final volume of carbonate formed, it is estimated that only ~4% of the brucite in this field-of-view would be required to react to produce

this mass of carbonate assuming stiochiometric lansfordite was formed. The MWI for the other frames could then be calculated using the same brucite mass determined at 245 min. The BET surface area of the brucite and the calculated volume of water present in each image were then used to estimate the MWI at each time point. These calculations revealed that the carbonate growth rate was not constant throughout the experiment, but tended to increase over time, before declining after the majority of water was lost to evaporation (Fig. 7A). The initial increase in growth rate is coincident with an increase in MWI, though it cannot be determined with certainty the causal relationship between these variables with the available data. Other factors, such as degree of supersaturation with respect to the carbonate mineral, may also have changed over time. Moreover, the decline in rate between 215 and 245 minutes despite a continued increase in MWI confirms that there are additonal processes governing reaction rate, highlighting the complexity of rate-controlling factors in such evaporative environments.

3.4 Force balance analysis

Dramatic increases in the MWI in the vicinity of the gas-water interface were observed during evaporation in all experiments due to entrainment of brucite particles by the retreating interface. To ascertain whether this process is likely to occur in 3-dimensional natural and anthropogenic porous media, and the range of grain sizes that would be impacted, we assessed the mobility of grains in the range of 10 to 1000 μm by conducting a force balance analysis. The entrainment of the particles by the interface is attributed to the surface tension force of the interface; whether the particles are entrained

by this force will depend on the balance between the surface tension force and resistive forces. The resistive forces (F_R) for grains between 10 to 1000 μm are dominated by contact and weight forces, while for grains smaller than about 10 μm, resistive forces are dominated by electrostatic interactions (Santamarina, 2003). In sediments and soils, grains, both large and small, that form the skeletal framework bearing the weight of the overlying sediment column will have larger resistive forces that are unlikely to be overcome by surface tension in normal circumstances. The following force balance analysis therefore applies only to non-skeletal grains.

The threshold grain size (L_T) for particle movement is that for which the resistive force is balanced by the surface tension exerted by the retreating meniscus (F_M). Grains smaller than L_T will be swept up by the retreating meniscus, while larger grains will be pinned by resistive forces.

The resistive forces based on the friction on the base of a mineral cube of grain size L can be approximated as:

$$F_R = \mu g \rho L^3 \qquad \text{Eq. 3}$$

where μ is the coefficient of friction, ρ is mineral density, and g is gravitational acceleration. The force exerted by the retreating meniscus can be related to the force balance at the water-air-mineral interface as:

$$F_M = F_{ls} - F_{sa} = \gamma L \cos\theta \qquad \text{Eq. 4}$$

where γ is the air-water surface tension, θ is the mineral-water contact angle, and F_{ls} and F_{sa} are forces defined in Figure 8 (DeMarsily, 1986). A constant contact angle was

assumed. The threshold grain size (L_T) for particle mobility is then the length-scale at which these two forces balance:

$$L_T = \left(\frac{\gamma \cos\theta}{\mu\rho g}\right)^{1/2} \qquad \text{Eq. 5}$$

Using values for common mineral grains (γ = 72 mN m^{-1}, Pallas and Harrison, 1990; θ = 40°, Espinoza and Santamarina, 2010; μ = 0.45, Lambe and Whitman, 1969; ρ = 2700 kg m^{-3}), the threshold length scale is 2.2 mm – an unattainably large grain size within the microfluidic model. The implication is that sand-sized and finer particles that are not load-bearing can be mobilized by a retreating meniscus, consistent with behavior observed in the microfluidics experiments, provided they are smaller than the pore throats. A wetted contact between mobile and skeletal grains would reduce the resistive force through buoyancy and a reduction in the coefficient of friction.

This simplified analysis differentiates the entrainment of particles by a retreating meniscus from the migration of particles laterally along the meniscus or within the pore fluid, towards the meniscus (*e.g.*, the coffee ring effect; Yunker et al., 2011), which is commonly observed during unconstrained droplet evaporation. The observation from our experiments that particles in the interior of the water-filled pores are generally immobile (*e.g.*, Fig. 6) is consistent with the dominant resistive forces to particle migration being contact rather than electrostatic forces. A similar phenomenon has recently been reported during unconstrained droplet evaporation of NaCl-bearing solutions, wherein newly-precipitated crystals of NaCl are mobilized towards the interior of the droplet due to capillary forces at the solid surface (Shahidzadeh et al., 2015). In more complex 3-dimensional media, wherein complicated drying patterns can develop (Vorhauer et al.,

2015) including the isolation and pinning of menisci, a number of forces in addition to the particle entrainment observed in our experiments may be expected.

4. Discussion

Injection of pure CO_2 gas into micromodels induced evaporation of water, dissolution of brucite, and precipitation of prismatic nesquehonite [$MgCO_3 \cdot 3H_2O$] crystals and other Mg-carbonate minerals (Figs. 2 and 3). Brucite particles dissolved (SI Video S1) and drove pore fluid to chemical saturation with Mg-carbonate minerals. These observations are consistent with the replacement of brucite by carbonate minerals as has been documented in bench-scale experiments and inferred from weathering of industrial wastes under similar geochemical conditions (Assima et al., 2014a, 2014b, 2012; Bea et al., 2012; Harrison et al., 2016, 2015, 2013; Hövelmann et al., 2012; Wilson et al., 2014). In the micromodel, and by inference in the shallow subsurface of Earth, interfaces between gas, liquid, and solid are mobile and exert a first order control on reactivity and hence element transport. We differentiate between the gas-water interfacial area (GWI), gas-mineral interfacial area (GMI), and mineral-water interfacial area (MWI) in Figure 2B. The mineral-water interfacial area is defined as the reactive mineral surface area per unit volume of water, the gas-mineral interfacial area is the mineral surface area in effectively dry pores, and the gas-water interfacial area is the surface area of the gas-water interface. Light microscopy revealed that evaporative water loss drove changes to the GWI and GMI, and that the entrainment of mineral grains by the retreating water menisci resulted in order-of-magnitude changes to the local volume-specific MWI, as estimated by image analysis with ImageJ (SI Videos S1-S2; Figs. 5 and 9).

4.1 Interface control on reaction progress/carbonate growth

Many mineral reactions proceed via dissolution and precipitation mechanisms in which aqueous solutions play a critical role. This is evident in our experiments wherein brucite in dry pores remained visibly unreacted, whereas hydrated carbonate precipitates were abundant in water filled pores (Fig. 2E; SI Video S1), demonstrating that the GMI is relatively unreactive. The experiments revealed that in nearly all occurrences of nesquehonite, the size, lateral extent, and morphology of crystals was limited by the location of the GWI (Fig. 2A, C). Only in large, connected, water-filled zones was nesquehonite precipitation not interface-limited (Fig. 2D). The micromodel experiments also revealed a propensity for formation of carbonate reaction products in areas of higher brucite abundance, *i.e.*, "mineral-buffered" zones (Fig. 2E; SI Video S1). Time-lapse images clearly demonstrate the absence of visible carbonation in a brucite-poor water-filled zone in contrast to abundant nesquehonite precipitation in an adjacent, comparatively brucite-rich water-filled zone (Fig. 2E; SI Video S1). This is attributed to the higher MWI, which allows rapid dissolution due to abundant mineral surface area, contributes a higher density of nucleation sites, and provides greater pH buffering capacity that promotes both increased CO_2 uptake into solution and carbonate precipitation. Geochemical models predict that with low MWI, even complete dissolution of the available brucite may not be sufficient to induce formation of carbonate precipitates, a likely explanation for the lack of carbonation in the brucite-poor, "fluid-buffered" zone (Fig. 10).

4.2 Evaporation-driven particle migration

Particle entrainment by moving water menisci during evaporation may enhance coupled mineral dissolution-precipitation reactions by increasing the MWI (Fig. 5). During evaporation, mineral particles were entrained behind the retreating fluid menisci, rather than being left behind in dry pores where they would be much less reactive (Figs. 2F, 6, and 9; SI Video S1). Mobility of mineral grains can occur if the surface tension forces exerted by the air-water meniscus at the mineral interface exceed the contact forces between the mineral grains. The force balance analysis indicated that sand and silt sized mineral grains can be mobile in normal soil conditions (Fig. 8), provided they are smaller than the pore diameter. Particle entrainment by mobile fluid menisci has been posited as an explanation for changes in physical structure and strength of agricultural soils upon wetting/drying. Textures consistent with this process have been observed in soils and bench-scale experiments (Fig. 2G, H) (Bresson and Moran, 1995; Harrison et al., 2015; Kemper and Rosenau, 1984; Mullins et al., 1987). Soils in arid and semi-arid environments are particularly susceptible, and tend to form hard surface crusts that may decrease infiltration of water, enhance erosion, and inhibit root growth (Bresson and Moran, 1995; Mullins et al., 1987). The observations of NaCl precipitates being mobilized by the gas water interface of evaporating salt solutions (Shahidzadeh et al., 2015) suggests this process may also govern the location of precipitates in unsaturated porous media. Although substantial research has been devoted to understanding the physical dynamics of drying in porous media, the more complex impacts, such as the advective transport of solutes and particle migration have not been fully addressed (Prat, 2011). To our knowledge, the relevance of these processes to larger scale mineral

weathering in the natural environment, and their potential impact on local fluid chemistry and reaction rate has not been assessed. The primary reactive phases in soils (*e.g.*, feldspars) that control global element fluxes are likely to be within the size range of particles affected by these particle entrainment processes.

Recent advances in pore-scale numerical modeling reveal that heterogeneity in physical pore structure can alter mineral dissolution rates (Molins et al., 2012). Physically, both the bulk pore structure and the local GWI are changed. Porosity is augmented in areas that dry out, increasing the relative permeability for gas flow, while the collection of fine particles in the water-filled zones could decrease permeability to water upon rewetting. In particular, the mobilization of fine particulates may tend to clog pores and pore throats, a phenomenon not noted in the micromodels owing to the relatively large pore throats in comparison to finer-grained porous media. Water recharge may remobilize particles in some circumstances (Lazouskaya et al., 2013), although the formation of mineral cement between grains would limit their remobilization (Harrison et al., 2015; Fig. 2G). The extent to which particles are mobilized will also depend on the relative size of mobile particles compared to pore diameters. Larger grains may tend to be less mobile due pore size restrictions between skeletal grains despite the potential to be entrained by the fluid meniscus.

4.3 Dynamic evolution of reaction system

Particle entrainment also results in a dynamic evolution of the chemical environment due to changes in mineral distribution, partitioning the system into "fluid-buffered" and "mineral-buffered" environments. These pore-scale heterogeneities can

lead to the development of water chemistry microenvironments different than the bulk solution (Li et al., 2007), not unlike the effect of microbes that change localized reaction rates by orders of magnitude (*e.g.*, Mielke et al., 2003). During evaporation from a 5 wt.% brucite slurry, the MWI was estimated to increase by approximately two orders of magnitude, based on image analysis (Fig. 6). Simple batch geochemical modeling of $[HCO_3^-]$-dependent brucite dissolution suggests that carbonation rates may be increased by a similar magnitude if rates are assumed to depend on local mineral surface area (Fig. 7A). Although this is a simplification, the carbonate growth rate observed experimentally is consistent with this result at early time (Fig. 7A, SI Video S2). Rates predicted by models and estimated from experiments differ significantly in absolute value, likely due to uncertainties in the estimation of brucite surface area and lansfordite volume in the experimental water-filled pore volume. However, it is expected that this uncertainty results in a systematic error (*i.e.*, a similar magnitude for each experimental time point), therefore the change in rate as a function of MWI still provides useful information. The decline in rate between 215 and 245 min (Fig. 7A) despite the continued increase in MWI suggests there are additional controls on reaction rate. Changes in reaction rate over time cannot solely be attributed to an increase in MWI, nor can a causal link definitively be drawn.

Nevertheless, there are additional intriguing consequences of the dynamic MWI. The increase in MWI triggered by particle movement may drive "brucite-poor," fluid-buffered zones into the more reactive "brucite-rich," mineral-buffered field, enhancing overall reactivity of the system as evaporation progresses. Of particular consequence is that an increased MWI in fluid-buffered microenvironments could stimulate carbonation

in previously unreactive pores. Thus particle mobility may initiate reaction in otherwise unreactive microenvironments. For example, Assima et al. (2012) observed that carbonation reaction in periodically wetted brucite-rich mine wastes was double that of experiments in which the same volume of water was introduced in a single wetting event. Manipulation of these processes could lead to improved control of mineral reactivity in agriculture and industrial processes such as for carbon sequestration. Rates of fertilizer and mineral dissolution could be optimized by tailoring wetting/drying cycles to increase the MWI.

The dynamic evolution of the MWI in soils in a changing climate may likewise lead to changes in chemical weathering fluxes in the vadose zone and solute release to river catchment areas. The effect of the changing MWI on mineral reaction rate will depend on the relative rate of attachment/detachment of ions at the mineral surface during dissolution/precipitation ("reaction-controlled" if rate-limiting) and the timescale of reactant/product transport ("transport-controlled"). In this context, a transport-controlled regime is at local equilibrium. The dimensionless Damköhler number (Da), can be used to distinguish between these regimes, and is defined as the ratio of the timescale of transport to the timescale of reaction (Steefel and Maher, 2009). The Da is related to the MWI as follows (Equation 6):

$$\mathrm{Da} = \frac{t_{adv}\, k\, \mathrm{MWI}}{C_{eq}} \quad \text{Eq. 6}$$

where t_{adv} is the advective time scale (residence time) of the fluid (s), k is the kinetic dissolution rate constant (mol m^{-2} mineral s^{-1}), C_{eq} is the solubility of the mineral phase (mol m^{-3} fluid), and MWI is in units of m^2 mineral m^{-3} fluid. As Da is proportional to

MWI, particle movement could shift the overall control of the reaction (Fig. 7B). Although our experiments were specifically designed to remain reaction-controlled, a three order of magnitude increase in Da indicates that a transition from reaction to transport control could be achieved, for example, via adjustment of the CO_2 supply rate (Fig. 7B).

4.4 Implications for solute transport and CO_2 uptake

At the transport timescale typical of soil moisture in the unsaturated zone (~10^6 s) (Stewart and McDonnell, 1991), reaction of the common, less reactive, minerals quartz and anorthite may change from reaction- to transport-controlled as a function of the MWI (Fig. 7B). In contrast, calcite dissolution remains transport-controlled over a large range of MWI. The net solute flux derived from a catchment depends on the reaction regime (Maher, 2011): solute flux will be increased disproportionately for transport-controlled regimes (Tipper et al., 2006). For example, Tipper et al. (2006) attribute seasonal variation in dissolved loads of river systems to the combined influence of transport-controlled carbonate dissolution, which will vary strongly between high and low runoff periods, and reaction-controlled silicate dissolution, which is more strongly influenced by the fluid residence time. Figure 7 implies that under the influence of extreme wetting and drying cycles, as might be induced by climate change, some silicate minerals have the possibility to switch from reaction-controlled to transport-controlled, at least locally, which in turn will affect solute fluxes and seasonal variations thereof. Interestingly, particle movement-induced shifts between “fluid-buffered” and “mineral-buffered” conditions could alter the solute flux derived from chemical weathering. As observed in the experiments, at low MWI secondary phases may not be chemically saturated,

reducing the solute flux. If the net effect of extreme wetting/drying cycles is to increase MWI, catchments may be driven towards "chemostatic" behavior, (Maher, 2011), thus increasing solute fluxes derived from chemical weathering and the capture of atmospheric CO_2.

5. Conclusions

The experiments provided unique insight into processes governing the gas-water-mineral interactions that occur in porous media undergoing evaporation, gas exchange, and mineral dissolution-precipitation. Three key interfaces were observed to control reaction at the pore-scale: 1) the gas-water interface (GWI), 2) the mineral-water interface (MWI; defined here as the ratio of mineral surface area to fluid volume), and 3) the gas-mineral interface (GMI). The location of the GWI was shown to impact the location and morphology of secondary carbonate minerals, suggesting water content and distribution will play a role in reaction-induced permeability changes. Water is the wetting fluid in these systems, therefore there was unlikely a true gas-mineral interface. However, particles residing in pores without visible water were defined to effectively comprise the GMI, and were not observed to react with CO_2 to produce visible precipitates at the scale of observation. Conversely, water-filled pores with high MWI were observed to readily facilitate precipitation of secondary carbonate minerals. Whether these precipitates form is dependent on the magnitude of the MWI; pore water in zones with low MWI may never reach saturation with respect to secondary minerals, whereas precipitation is facilitated in zones with high MWI. The magnitude of the MWI

was highly dynamic during evaporation, due not only to water loss, but the entrainment of reactive particles by the mobile gas-water interface, a consequence of surface tension. Although the net effect of particle entrainment processes on bulk reaction rates in porous media requires additional investigation, our experiments demonstrated that particle entrainment could significantly impact mineral-fluid reaction rates and distribution at the pore-scale. We posit two key outcomes of particle entrainment on mineral-fluid reaction as observed in our experiments: 1) localized increases in MWI could stimulate precipitation in previously "unreactive" pores, and 2) reactive particles are preferentially kept within water-filled pores where they are more reactive compared to "dry" pores. The pore-scale heterogeneities in reactive mineral distribution, their dynamic nature, and their impact on the size, distribution, and existence of secondary precipitates mean that reaction rates are likely to be highly heterogeneous and difficult to predict in shallow subsurface environments subjected to repeated wetting and drying cycles, which may contribute to a well-known discrepancy between mineral reaction rates measured in field versus laboratory settings (White and Brantley, 2003). As wetting and drying cycles are expected to continue to evolve with global climate change, further investigation of the impacts of wetting and drying on mineral reactions is merited.

Acknowledgments

We thank Percy Graham for assistance with microscopy, and Phong Nguyen for manufacturing the micromodel. Jed Harrison and Neda Nazemifard provided insight into microfluidics and particle movement. David Parkhurst and Christian Schoof provided

advice regarding geochemical modeling and force balance calculations, respectively. We would like to thank Kate Maher, Marjorie Schulz, Jennifer Harden, and Andrew Putnis for helpful discussion. Funding was provided by a Geological Society of America student research grant and Natural Science and Engineering Research Council of Canada (NSERC) postgraduate scholarship to ALH, and NSERC and Carbon Management Canada research grants to GMD. WS thanks DuPont Canada for partially funding a Queen Elizabeth II Scholarship in Science and Technology.

References

Aagaard, P., Helgeson, H.C., 1982. Thermodynamic and kinetic contraints on reaction rates among minerals and aqueous solutions. I. Theoretical considerations. Am. J. Sci. 282, 237–285.

Abràmoff, M.D., Magalhães, P.J., Ram, S.J., 2004. Image Processing with ImageJ. Biophotonics Int. 11, 36–42.

Akao, M., Iwai, S., 1977. The hydrogen bonding of hydromagnesite. Acta Crystallogr. Sect. B 33, 1273–1275.

Assima, G.P., Larachi, F., Beaudoin, G., Molson, J.W., 2012. CO_2 sequestration in chrysotile mining residues - Implication of watering and passivation under environmental conditions. Ind. Eng. Chem. Research. 51, 8726–8734.

Assima, G.P., Larachi, F., Molson, J., Beaudoin, G., 2014a. Comparative study of five Québec ultramafic mining residues for use in direct ambient carbon dioxide mineral sequestration. Chem. Eng. J. 245, 56–64.

Assima, G.P., Larachi, F., Molson, J., Beaudoin, G., 2014b. Impact of temperature and oxygen availability on the dynamics of ambient CO_2 mineral sequestration by nickel mining residues. Chem. Eng. J. 240, 394–403.

Batchelder, D.N., Simmons, R.O., 1964. Lattice constants and thermal expansivities of silicon and of calcium fluoride between 6° and 322°K. J. Chem. Phys. 41, 2324.

Bea, S.A., Wilson, S.A., Mayer, K.U., Dipple, G.M., Power, I.M., Gamazo, P., 2012. Reactive transport modeling of natural carbon sequestration in ultramafic mine tailings. Vadose Zone Journal 11.

Blowes, D.W., Jambor, J.L., 1990. The pore-water geochemistry and the mineralogy of the vadose zone of sulfide tailings, Waite Amulet, Quebec, Canada. Appl. Geochemistry 5, 327–346.

Boyd, V., Yoon, H., Zhang, C., Oostrom, M., Hess, N., Fouke, B., Valocchi, A.J., Werth, C.J., 2014. Influence of Mg^{2+} on $CaCO_3$ precipitation during subsurface reactive transport in a homogeneous silicon-etched pore network. Geochim. Cosmochim. Acta 135, 321–335.

Brady, P. V., Walther, J. V., 1990. Kinetics of quartz dissolution at low temperatures. Chem. Geol. 82, 253–264.

Brantley, S.L., White, A.F., 2009. Approaches to Modeling Weathered Regolith. Rev. Mineral. Geochemistry 70, 435–484.

Bresson, L.M., Moran, C.J., 1995. Structural change induced by wetting and drying in seedbeds of a hardsetting soil with contrasting aggregate size distribution. Eur. J. Soil Sci. 46, 205–214.

Bruker AXS, 2004. Topas V.3.0: General Profile and Structural Analysis Software for Powder Diffraction Data. Bruker AXS, Germany. Powder Diffr.

Bruker AXS, 2008. DIFFRACplus EVA 14 Release 2008.

Catti, M., Ferraris, G., Hull, S., Pavese, a., 1995. Static compression and H disorder in brucite, $Mg(OH)_2$, to 11 GPa: A powder neutron diffraction study. Phys. Chem. Miner. 22, 200–206.

Chou, L., Garrels, R.M., Wollast, R., 1989. Comparative study of the kinetics and mechanisms of dissolution of carbonate minerals. Chem. Geol. 78, 269–282.

DeMarsily, G., 1986. Quantitative hydrogeology. Academic Press, Inc., Orlando, Florida.

Dong, M., Cheng, W., Li, Z., Demopoulos, G.P., 2008. Solubility and stability of nesquehonite ($MgCO_3 \cdot H_2O$) in mixed NaCl + $MgCl_2$, NH_4Cl + $MgCl_2$, LiCl, and LiCl + $MgCl_2$ solutions. J. Chem. Eng. Data 53, 2586–2593.

Espinoza, D.N., Santamarina, J.C., 2010. Water-CO_2-mineral systems: Interfacial tension, contact angle, and diffusion – Implications to CO_2 geological storage. Water Resour. Res. 46, W07537.

Gualtieri, A.F., 2000. Accuracy of XRPD QPA using the combined Rietveld ± RIR method research papers. J. Appl. Crystallogr. 33, 267–278.

Gudbrandsson, S., Wolff-Boenisch, D., Gislason, S.R., Oelkers, E.H., 2014. Experimental determination of plagioclase dissolution rates as a function of its composition and pH at 22° C. Geochim. Cosmochim. Acta. 139, 154–172.

Harrison, A.L., Dipple, G.M., Power, I.M., Mayer, K.U., 2016. The impact of evolving mineral-water-gas interfacial areas on mineral-fluid reaction rates in unsaturated porous media. Chem. Geol. 421, 65–80.

Harrison, A.L., Dipple, G.M., Power, I.M., Ulrich Mayer, K., 2015. Influence of surface passivation and water content on mineral reactions in unsaturated porous media: Implications for brucite carbonation and CO_2 sequestration. Geochim. Cosmochim. Acta 148, 477–495.

Harrison, A.L., Power, I.M., Dipple, G.M., 2013. Accelerated carbonation of brucite in mine tailings for carbon sequestration. Environ. Sci. Technol. 47, 126–134.

Hövelmann, J., Putnis, C. V., 2016. In situ nanoscale imaging of struvite formation during the dissolution of natural brucite: Implications for phosphorus recovery from wastewaters. Environ. Sci. Technol. 50, 13032–13041.

Hövelmann, J., Putnis, C. V, Ruiz-Agudo, E., Austrheim, H., 2012. Direct nanoscale observations of CO_2 sequestration during brucite [$Mg(OH)_2$] dissolution. Environ. Sci. Technol. 46, 5253–5260.

IPCC, 2013. Climate change 2013: The physical science basis. Working group 1 contribution to the fifth assessment report of the Intergovernmental Panel on Climate Change. Cambridge University Press, Cambridge, UK and New York.

Kemper, W.D., Rosenau, R.C., 1984. Soil cohesion as affected by time and water content. Soil Sci. Soc. Am. J. 48, 1001–1006.

Kim, M., Sell, A., Sinton, D., 2013. Aquifer-on-a-Chip: understanding pore-scale salt precipitation dynamics during CO_2 sequestration. Lab Chip 13, 2508–2518.

Lambe, W.T., Whitman, R.V., 1969. Soil Mechanics. John Wiley & Sons. 553 p.

Lazouskaya, V., Wang, L.-P., Or, D., Wang, G., Caplan, J.L., Jin, Y., 2013. Colloid mobilization by fluid displacement fronts in channels. J. Colloid Interface Sci. 406, 44–50.

Li, L., Peters, C.A., Celia, M.A., 2006. Upscaling geochemical reaction rates using pore-scale network modeling. Adv. Water Resour. 29, 1351–1370.

Li, L., Peters, C.A., Celia, M.A., 2007. Effects of mineral spatial distribution on reaction rates in porous media. Water Resour. Res. 43, W01419.

Li, L., Steefel, C.I., Yang, L., 2008. Scale dependence of mineral dissolution rates within

single pores and fractures. Geochim. Cosmochim. Acta 72, 360–377.

Maher, K., 2011. The role of fluid residence time and topographic scales in determining chemical fluxes from landscapes. Earth Planet. Sci. Lett. 312, 48–58.

Maher, K., Steefel, C.I., White, A.F., Stonestrom, D.A., 2009. The role of reaction affinity and secondary minerals in regulating chemical weathering rates at the Santa Cruz Soil Chronosequence, California. Geochim. Cosmochim. Acta 73, 2804–2831.

Manning, D.A.C., 2008. Biological enhancement of soil carbonate precipitation: Passive removal of atmospheric CO_2. Mineral. Mag. 72, 639–649.

Markgraf, S., Reeder, R.J., 1985. High-temperature structure refinements of calcite and magnesite. Am. Mineral. 70, 590–600.

McKinley, J.P., Zachara, J.M., Liu, C., Heald, S.C., Prenitzer, B.I., Kempshall, B.W., 2006. Microscale controls on the fate of contaminant uranium in the vadose zone, Hanford Site, Washington. Geochim. Cosmochim. Acta 70, 1873–1887.

Mellini, M., Viti, C., 1994. Crystal structure of lizardite-1T from Elba, Italy. Am. Mineral. 79, 1194–1198.

Mielke, R.E., Pace, D.L., Porter, T., Southam, G., 2003. A critical stage in the formation of acid mine drainage: Colonization of pyrite by *Acidithiobacillus ferrooxidans* under pH-neutral conditions. Geobiology 1, 81–90.

Molins, S., Trebotich, D., Steefel, C.I., Shen, C., 2012. An investigation of the effect of pore scale flow on average geochemical reaction rates using direct numerical simulation. Water Resour. Res. 48, W03527.

Mullins, C.E., Young, I.M., Bengough, A.G., Ley, G.J., 1987. Hard-setting soils. Soil

Use Manag. 3, 79–83.

Olowe, A., 1995. Crystal structures of pyroaurite and sjogrenite. Adv. X-ray Anal. 38, 749–755.

Pallas, N.R., Harrison, Y., 1990. An automated drop shape apparatus and the surface tension of pure water. Colloids and Surfaces 43, 169–194.

Parkhurst, D.L., Appelo, C.A.J., 2013. Description of Input and Examples for PHREEQC Version 3 — A Computer Program for Speciation , Batch-Reaction , One-Dimensional Transport , and Inverse Geochemical Calculations, in: U.S. Geological Survey Techniques and Methods, Book 6, Chap. A43. Denver, Colorado, p. 497.

Pokrovsky, O., Schott, J., 2004. Experimental study of brucite dissolution and precipitation in aqueous solutions: Surface speciation and chemical affinity control. Geochim. Cosmochim. Acta 68, 31–45.

Pokrovsky, O.S., Golubev, S. V., Schott, J., 2005a. Dissolution kinetics of calcite, dolomite and magnesite at 25°C and 0 to 50 atm pCO_2. Chem. Geol. 217, 239–255.

Pokrovsky, O.S., Schott, J., Castillo, A., 2005b. Kinetics of brucite dissolution at 25°C in the presence of organic and inorganic ligands and divalent metals. Geochim. Cosmochim. Acta 69, 905–918.

Power, I.M., Harrison, A.L., Dipple, G.M., 2016. Accelerating mineral carbonation using carbonic anhydrase. Environ. Sci. Technol. 50, 2610–2618.

Power, I.M., Harrison, A.L., Dipple, G.M., Southam, G., 2013. Carbon sequestration via carbonic anhydrase facilitated magnesium carbonate precipitation. Int. J. Greenhouse Gas Control. 16, 145–155.

Power, I.M., Wilson, S.A., Harrison, A.L., Dipple, G.M., McCutcheon, J., Southam, G., Kenward, P.A., 2014. A depositional model for hydromagnesite-magnesite playas near Atlin, British Columbia, Canada. Sedimentology 61, 1701–1733.

Power, I.M., Wilson, S.A., Thom, J.M., Dipple, G.M., Gabites, J.E., Southam, G., 2009. The hydromagnesite playas of Atlin, British Columbia, Canada: A biogeochemical model for CO_2 sequestration. Chem. Geol. 260, 286–300.

Prat, M., 2011. Pore network models of drying, contact angle, and film flows. Chem. Eng. Technol. 34, 1029–1038.

Raudsepp, M., Pani, E., 2003. Application of Rietveld analysis to environmental mineralogy., in: Jambor, J.L., Blowes, D.W., Ritchie, A.I.. (Eds.), Environmental Aspects of Mine Wastes, 31, Mineralogical Association of Canada, Short Course Series, Ottawa, Ontario, Canada. Ottawa, pp. 165–180.

Ross, N.L., Reeder, R.J., 1992. High-pressure structural study of dolomite and ankerite. Am. Mineral. 77, 412–421.

Santamarina, J.C., 2003. Soil behavior at the microscale: Particle forces. Geotech. Spec. Publ. 25–26.

Shahidzadeh, N., Schut, M.F.L., Desarnaud, J., Prat, M., Bonn, D., 2015. Salt stains from evaporating droplets. Sci. Rep. 5, 10335.

Song, W., Kovscek, A.R., 2015. Functionalization of micromodels with kaolinite for investigation of low salinity oil-recovery processes. Lab Chip 15, 3314–3325.

Steefel, C.I., Maher, K., 2009. Fluid-rock interaction: A reactive transport approach. Rev. Mineral. Geochemistry 70, 485–532.

Stewart, M.K., McDonnell, J.J., 1991. Modeling base flow soil water residence times from deuterium concentrations. Water Resour. Res. 27, 2681–2693.

Ulven, O.I., Beinlich, A., Hovelmann, J., Austrheim, H., Jamtveit, B., 2017. Earth Planet. Sci. Lett. 468, 11–26.

Vorhauer, N., Wang, Y.J., Kharaghani, A., Tsotsas, E., Prat, M., 2015. Transp. Porous Med. 110, 197–223.

White, A.F., Brantley, S.L., 2003. The effect of time on the weathering of silicate minerals: why do weathering rates differ in the laboratory and field? Chem. Geol. 202, 479–506.

Wilson, S.A., Raudsepp, M., Dipple, G.M., 2006. Verifying and quantifying carbon fixation in minerals from serpentine-rich mine tailings using the Rietveld method with X-ray powder diffraction data. Am. Mineral. 91, 1331–1341.

Yoon, H., Valocchi, A.J., Werth, C.J., Dewers, T., 2012. Pore-scale simulation of mixing-induced calcium carbonate precipitation and dissolution in a microfluidic pore network. Water Resour. Res. 48, W02524.

Yunker, P.J., Still, T., Lohr, M.A., Yodh, A.G., 2011. Suppression of the coffee-ring effect by shape-dependent capillary interactions. Nature 476, 308–311.

Zhang, J., 2010. Lattice Boltzmann method for microfluidics: Models and applications. Microfluid. Nanofluidics 10, 1–28.

Zhao, L., Sang, L., Chen, J., Ji, J., Teng, H.H., 2010. Aqueous carbonation of natural brucite: Relevance to CO_2 sequestration. Environ. Sci. Technol. 44, 406–411.

Figure Captions

Figure 1. Schematic of the micromodel pore network. The inset figure illustrates the arrangement of the cylindrical glass pillars in three dimensions, which extended over the entire (~130 μm) depth of the micromodel.

Figure 2. Conceptual schematic and representative transmitted light and backscattered electron micrographs of brucite carbonation. Gas-filled areas are false colored in green. A) Prismatic nesquehonite. B) Conceptual model of key interfaces. The mineral-water interfacial area (MWI) is defined as the reactive mineral surface area per unit volume of water (red dashed line), the gas-mineral interfacial area (GMI) is the mineral surface area in effectively dry pores (green dashed line) and the gas-water interfacial area (GWI) is the surface area of the gas-water interface (blue dashed line). C) Nesquehonite precipitates in water-filled area with lateral growth limited by the gas-water interface. D) Abundant nesquehonite precipitates in a large, connected, water-filled zone. Inset showing a close-up of nesquehonite crystals in this zone. E) Nesquehonite precipitation in a brucite-rich, water filled zone (left-hand side; red dashed line) compared to lack of carbonation in a brucite-poor, water filled zone (right-hand side) and gas-filled, dry area (middle). F) Evidence of brucite entrainment by water menisci during evaporation (indicated by black arrows). The location of the GWI at an earlier time is indicated by the white dashed line and black arrows, whereas the GWI at the end of the experiment is indicated by a red arrow and the blue dashed line. G) Backscattered electron micrograph of reaction products from a bench scale brucite carbonation experiment (Harrison et al.,

2015) exhibiting textures consistent with particle entrainment by the mobile fluid meniscus. The epoxy-mineral interface, indicated by the blue arrow, is an approximate representation of the location of the GWI at the end of the experiment. H) Schematic representation of the key interfaces in (G). Dashed lines are color coded according to the scheme in (B), except the black dashed line, which represents the effectively inert quartz [SiO_2]-water interface. All scale bars are 200 μm.

Figure 3. Brightfield light and scanning electron micrographs of lansfordite crystals. A) Brightfield image of rhombohedral crystal formed during the first micromodel experiment in a water filled zone. B) Scanning electron micrograph of a lansfordite crystal synthesized in our laboratory from natural water collected from a Mg- and CO_2-rich wetland pond in Atlin, British Columbia. Scale bars are 200 μm.

Figure 4. Raman spectra of reaction products from five locations within the micromodel following the second (8 h) experiment. Characteristic peaks of brucite (Brc), nesquehonite (Nsq), dolomite (Dol), dypingite (Dyp), and magnesite (Mgs) are identified. The inset figure shows a close up of the grey shaded region of spectrum 'Mar27-15.'

Figure 5. Image analysis of brucite slurry between two glass slides after 10 min of evaporation. A) Light micrograph of brucite slurry after 10 min of evaporation. B, C)

Subsections of equal size from a light micrograph of an initially 5 wt.% brucite slurry after 10 minutes of evaporation. (B) represents a "brucite-poor" zone from the undisturbed interior of the evaporating water volume, whereas (C) represents the vicinity of the gas-water interface, where particle entrainment is most extreme. (D) and (E) illustrate the areas that were calculated as water using ImageJ to determine the relative percent of water versus mineral in images (B) and (C), respectively. Pixels assigned as water are shaded red. The scale bar in (A) is 200 μm, whereas those in (B-E) are 20 μm.

Figure 6. Entrainment of brucite particles by the retreating water meniscus during evaporation. Initial brucite slurry (5 wt.%) (A) and brucite slurry following 10 minutes of evaporation (B) at room temperature between two glass slides, as observed using transmitted light microscopy. Circles indicate identical brucite particles before and after evaporation for spatial reference. Red circles show particles that remained stationary and the blue circle shows a particle that has been moved and rotated. Scale bars are 200 μm.

Figure 7. Modeled and experimental carbonation rate versus initial mineral-water interfacial area (MWI^0) and volume percent brucite (A) and Damköhler number (Da) versus MWI (B). Inset photomicrographs in (A) display examples of heterogeneity in brucite abundance in the evaporation experiment pictured in Figure 6. The experimental carbonation rates were estimated from Video S2. Lines in (B) were calculated using a transport timescale equal to the approximate residence time of soil moisture (~10^6 s;

Stewart and McDonnell, 1991), except for brucite, which was calculated based on the CO_2 velocity in the experimental systems. The residence time of CO_2 in the micromodels was ~10 s. The timescale of reaction was determined using geochemical modeling of kinetic dissolution of each mineral. It was defined as the time to reach 80% equilibrium (*i.e.*, a saturation index of -0.1) in order to simplify calculation of dissolution rates under close to equilibrium conditions, which are typically poorly understood. This approach effectively defines systems that are close to equilibrium as at equilibrium.

Figure 8. Schematic of force balance analysis on non-skeletal grains >10 μm. F_R is the resistive force, μ is the coefficient of friction, F_N is the normal force, F_M is the surface tension exerted by the retreating water meniscus, L is the mineral grain size, θ is the contact angle, and F_{ls}, F_{la}, and F_{sa} are the liquid-solid, liquid-air, and solid-air surface tensions, respectively.

Figure 9. Time series of light micrographs during the 8 h micromodel experiment illustrating the entrainment of brucite particles by the retreating gas-fluid interface. Micrographs captured at 250 min (A), 285 min (B), 355 min (C), and 360 min (D).

Figure 10. Lansfordite saturation as a function of mineral-water interfacial area (MWI) and brucite dissolution. Values were calculated using PHREEQC (Parkhurst and Appelo, 2013) and a [HCO_3^-]-dependent kinetic brucite dissolution rate law (Pokrovsky et al., 2005b).

Video Captions

Video S1. Brucite reaction in a brucite-rich, water filled zone compared to a brucite-poor, water filled zone, and gas-filled zones. The video consists of time lapse images taken at 5 minute intervals using a light microscope played at two frames per second (10 min experiment time per 1 s). The entire duration shown is ~7.3 h with a field of view of 3.4 mm × 2.2 mm. The scale bar is 200 μm. Black frames replace frames that have been removed due to technical problems with the microscope. A water-filled, brucite-rich zone is observed on the left-hand side of the video, whereas a comparatively brucite-poor water-filled zone is observed on the right-hand side of the video. Between the water-filled zones is a dry, gas-filled area within which are some brucite particles. The gas filled areas appear as a brighter grey that is separated from water-filled areas by the gas-water interface which appears as a dark black line that moves during evaporation. By the end of the video, the majority of the water has been removed via evaporation and incorporation into hydrated Mg-carbonate precipitates. Different behaviors are observed between the brucite-rich and brucite-poor zones. Although the disappearance of brucite particles due to dissolution is observed in both areas, the occurrence of carbonate precipitation is only visible in the brucite-rich zone. Red arrows indicate two occurrences of nesquehonite precipitation in the brucite-rich zone (left-hand side of the video). Similarly, no visible carbonate precipitation occurs within the dry, gas-filled zone between the water filled areas.

Video S2. Carbonate precipitation in a water-filled zone in a micromodel. The video consists of time lapse images taken at 5 minute intervals using a light microscope played

at two frames per second (10 min experiment time per 1 s). The entire duration shown is ~10 h with a field of view of 1.9 mm × 1.3 mm. The scale bar is 200 μm. Black frames replace frames that have been removed due to technical problems with the microscope. This video shows a single water filled area containing brucite particles. Brucite particles appear as black to dark grey. The gas-water interface appears as a dark black line that separates the water-filled pores from the brighter grey, gas-filled pores. A large crystal of hydrated Mg-carbonate is observed to precipitate in the water-filled zone as evaporation progresses. By the end of the video, the water has been nearly completed removed from the field of view via evaporation and incorporation into the hydrated Mg-carbonate phase.

Fig. 1

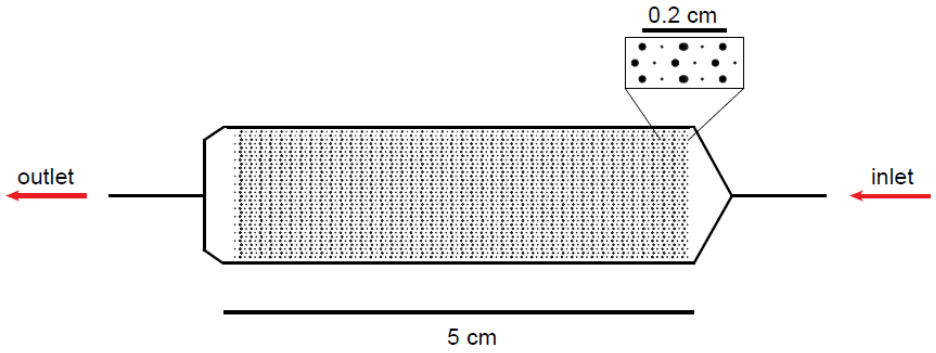

Fig. 2

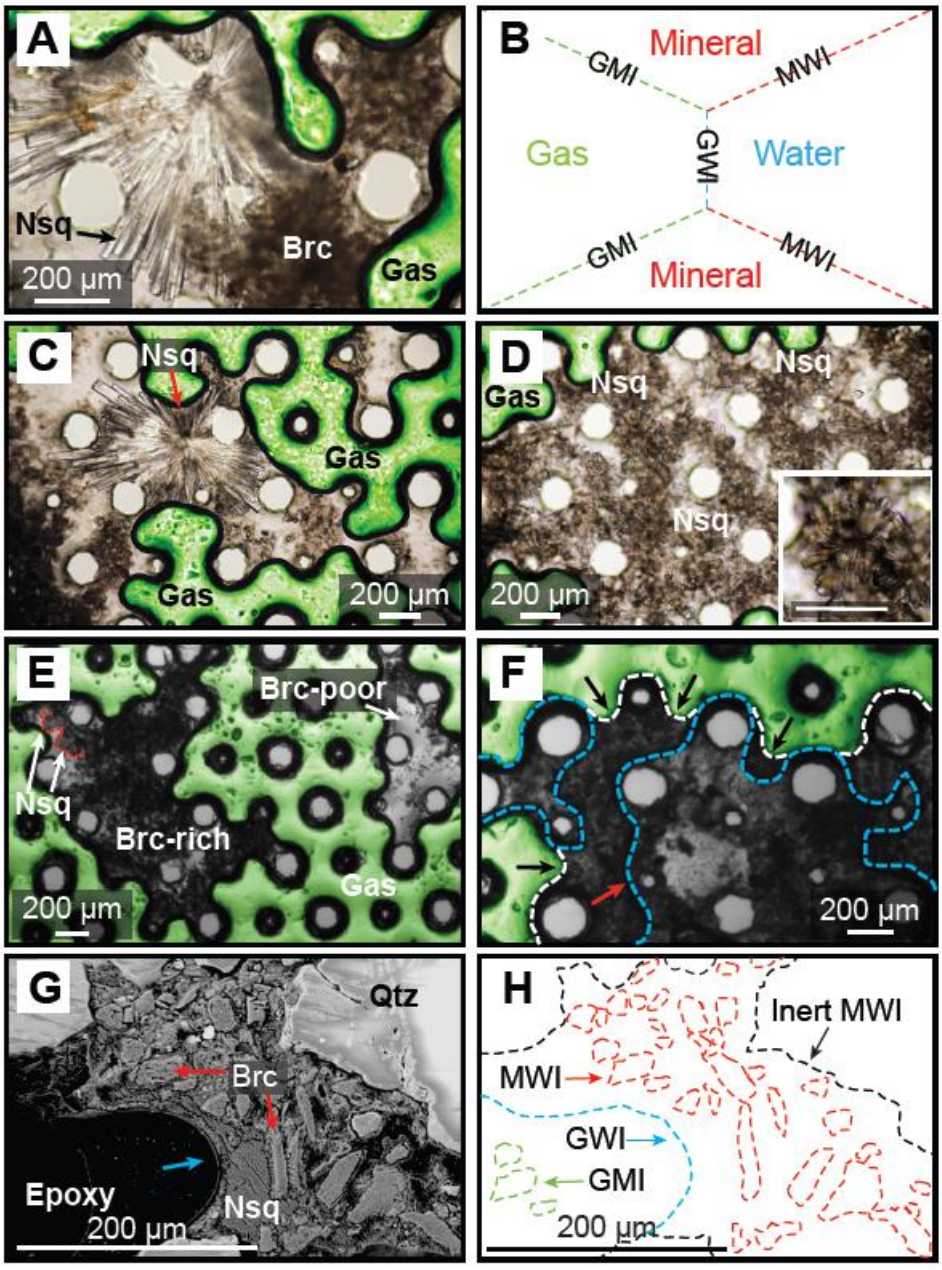

Fig. 3

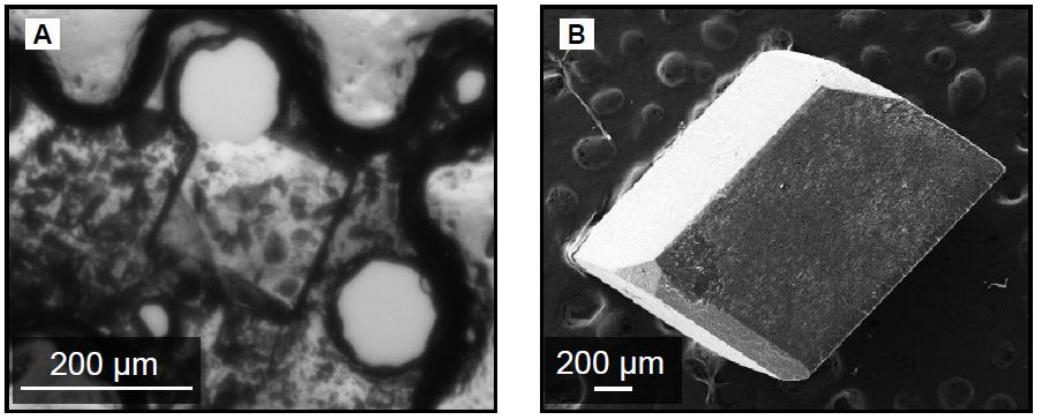

Fig. 4

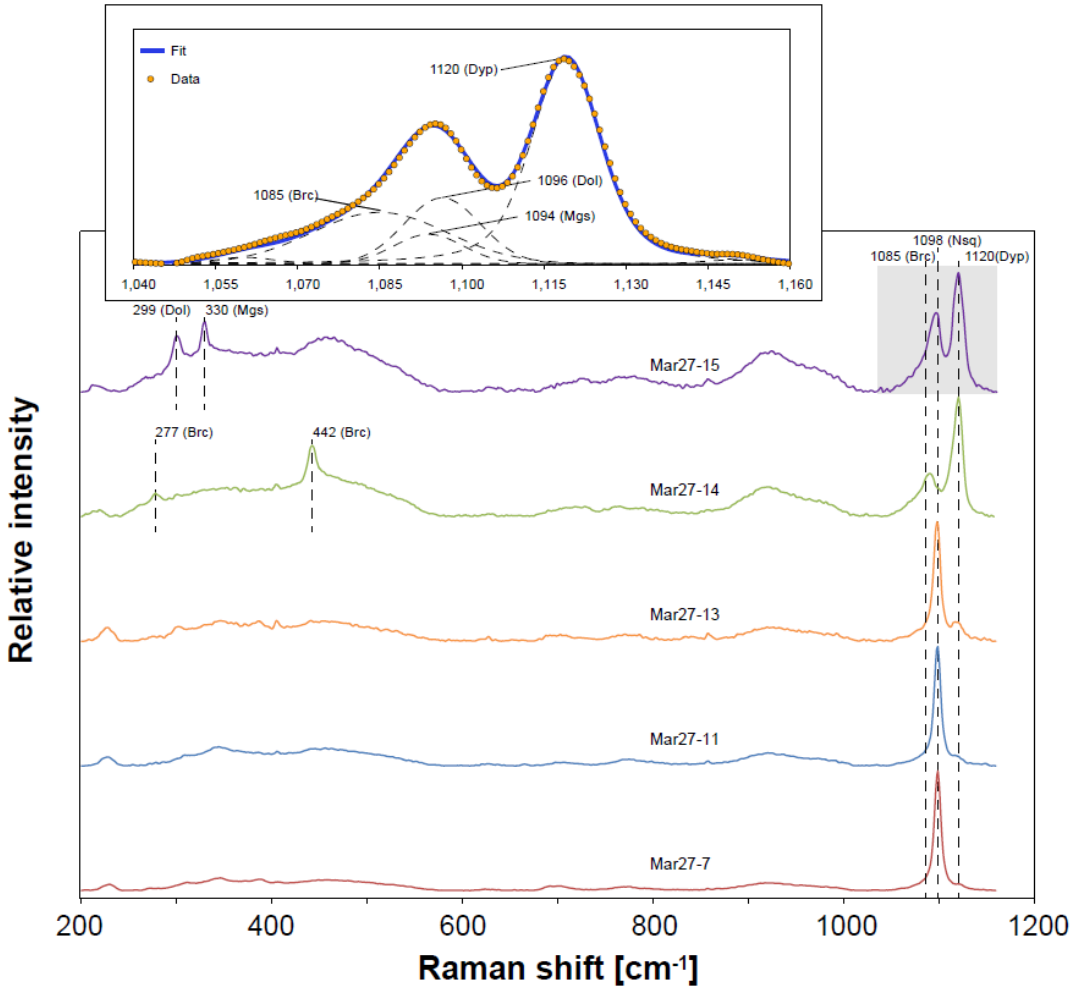

Fig. 5

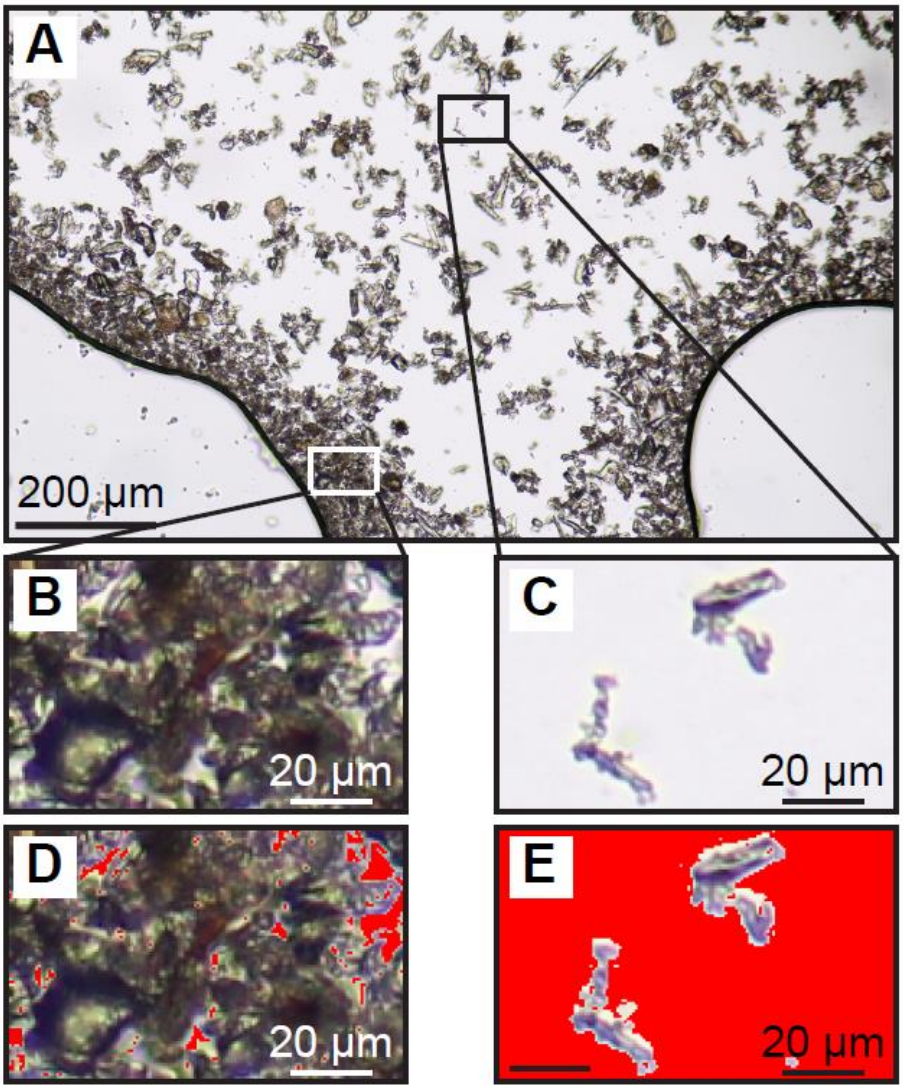

Fig. 6

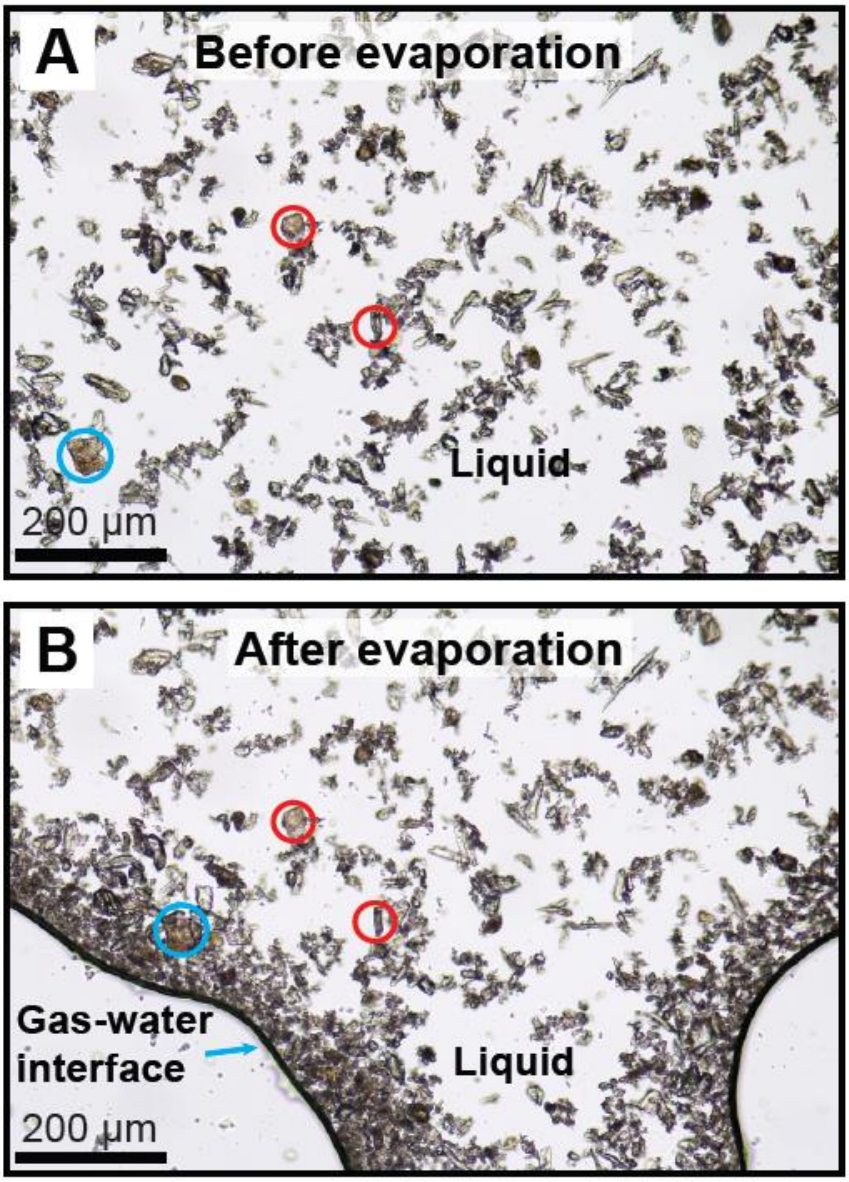

Fig. 7

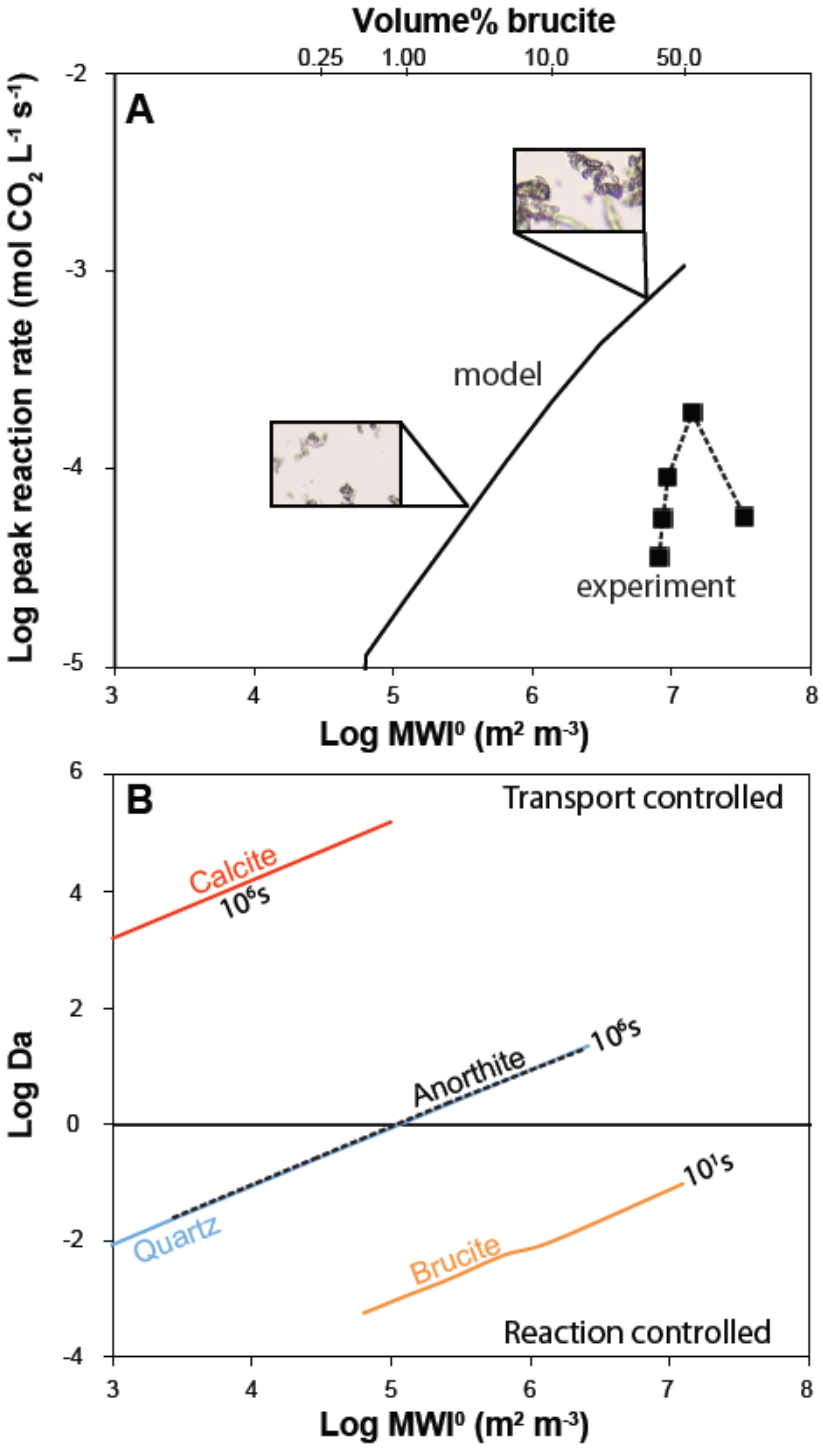

Fig. 8

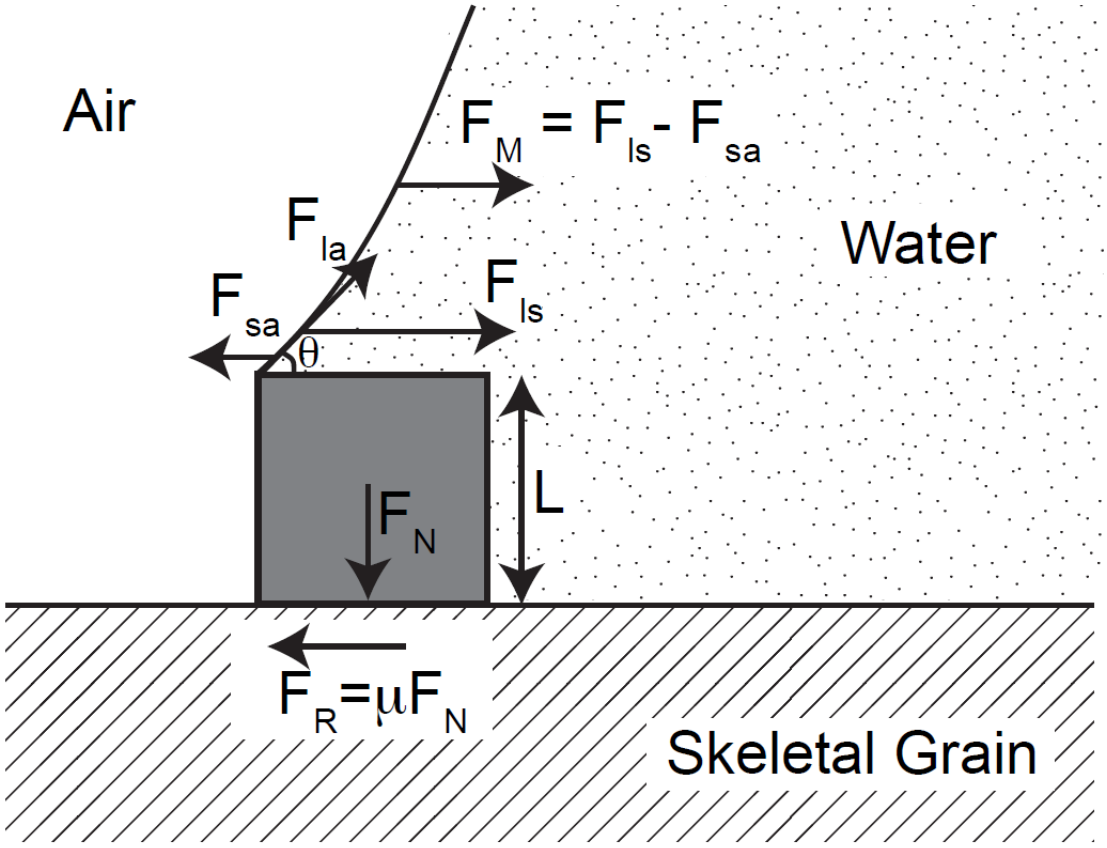

Fig. 9

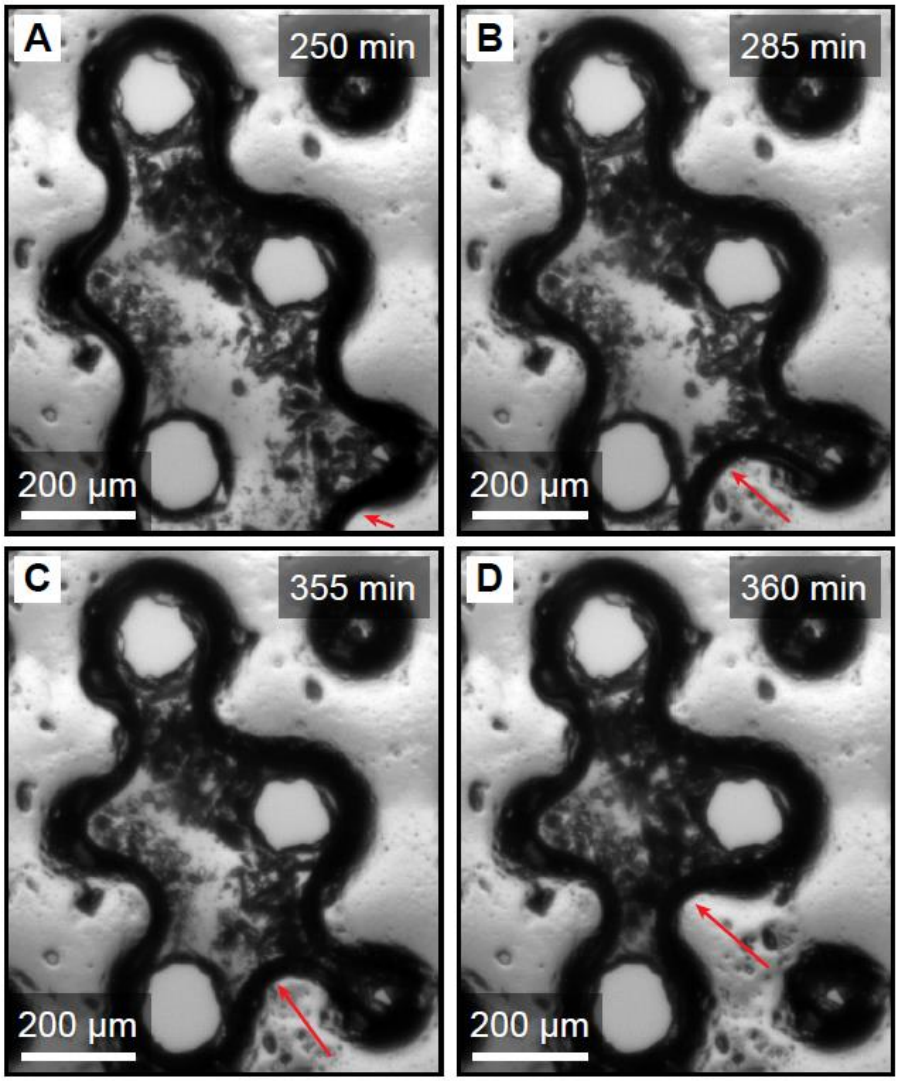

Fig. 10

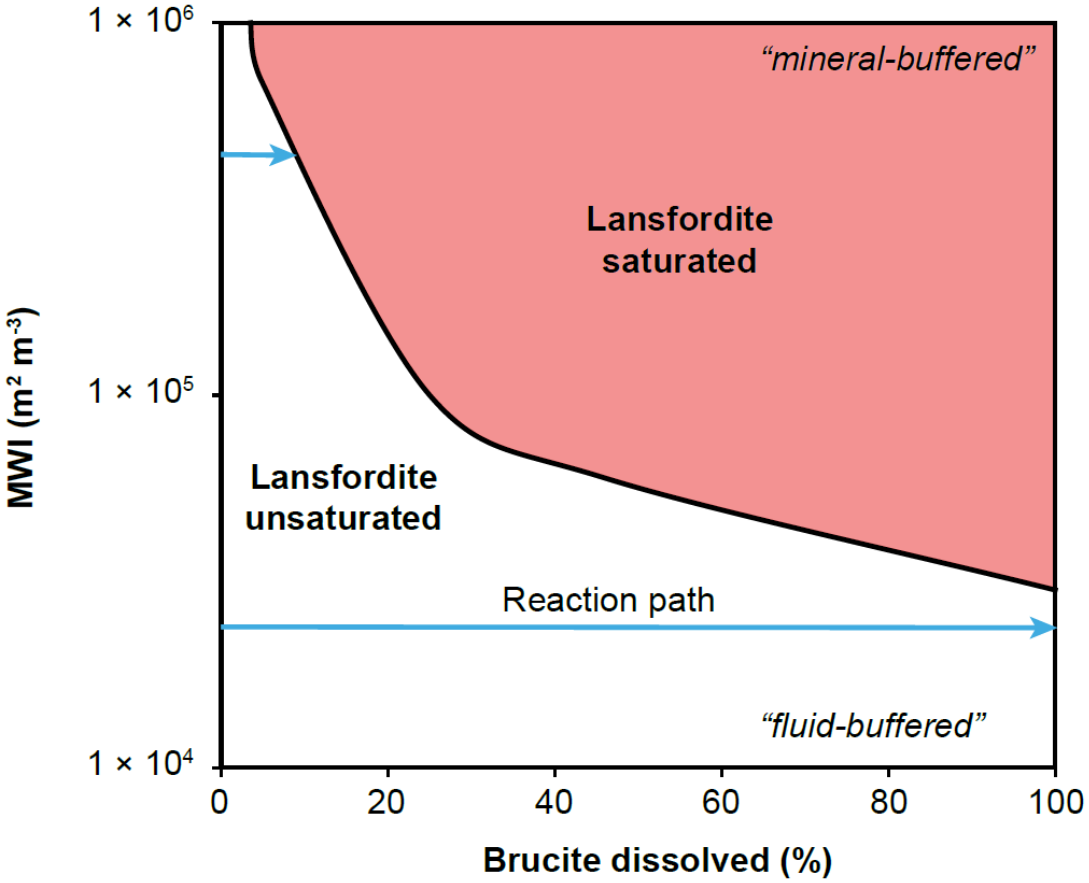

Graphical abstract